Highly Stable and Scalable Lithium Metal Anodes Enabled by a Lithiophilic SnO$_2$@Graphite Fiber Framework Design

Xiaojuan Qian,[a, b] Di Miao,[a] Xiaoping Lin,[c] Maohua Chen,[c] Yuansen Xie,[c] Jie Qu,*[a] Xingchao Tu,*[b] and Chao Lai*[b]

The uncontrollable growth of dendrites, infinite volume changes, low Coulombic efficiencies, and poor charging/discharging rates in lithium metal anodes have seriously hampered the further development of lithium metal batteries. Trapping lithium (Li) into rationally designed three-dimensional (3D) structured Li metal anodes in order to construct a 3D-Li framework is an effective approach to suppress the growth of Li dendrites. However, material inconsistencies and high costs still seriously limit practical applications. In this study, we describe the use of commercial low-cost graphite fiber (GF) as a suitable conformal scaffold for preparing a lithiophilic SnO$_2$@GF material using facile infiltration method. The lithiophilic 3D porous conductive framework allows homogeneous Li deposition on the surface of a structured electrode and accommodates the volume change during Li plating/stripping, leading to a significant boost in both the charging/discharging rates and cycling stability. This study highlights the significance of interface-related science and engineering in designing high-performance Li metal anodes, but also highlights the need for greater dedication to the construction of highly stable lithium anodes and high-energy density Li metal batteries in a low-cost manner.

Introduction

Lithium-ion batteries (LIBs) have occupied a tremendous market share since the 1990s owing to their use in portable electronic devices (typically, mobile phones and laptops) and electric vehicles (EVs).[1–3] To some extent, LIBs are reshaping communications and transportation in modern lifestyles.[4] Nevertheless, the improvements in energy density brought by LIBs are comparatively poor, and such graphite anode-based LIBs (theoretical capacity, 372 mAh g^{-1}) cannot fulfill the high energy density expectations of cutting-edge electronic devices.[5–7] Therefore, there is an urgent need to develop novel secondary battery systems that exceed conventional LIBs.[8,9]

The Li metal anode possesses an extremely high theoretical energy density of 3860 mAh g^{-1} and a low redox potential of −3.04 V (vs. standard hydrogen electrode);[10–12] thus, it has been proposed as an alternative ultimate anode to the current commercialized Li-ion battery system.[13] Unfortunately, the unexpected growth of Li dendrites during the cycling process can result in poor coulombic efficiency (CE), engendering serious safety concerns[14,15] and severely limiting the practical applications of Li metal-based batteries.[16–20]

In recent years, tremendous efforts have been made to solve the above mentioned problems by developing high-performance Li metal anodes, including modifying organic/aqueous electrolytes, engineering solid-state electrolytes, trapping Li into 3D conductive hosts, designing stable interfacial solid electrolyte interface (SEI) layers by understanding their structures and components, healing, eliminating, or controlling the growth direction of Li dendrites.[21–36] Among these approaches, the construction of 3D-structured electrodes is an efficient approach to regulating the electrical field distribution, decreasing local current densities, and suppressing Li dendrite growth,[37,38] which allows the volume expansion and shrinkage of Li during the plating/stripping process to be accommodated.[39] Owing to its lithium affinity, a lithiophilic 3D scaffold can absorb lithium-ion clusters, which can be uniformly distributed on the surface of the collector, leading to uniform lithium-ion deposition.[40,41] Doped graphene,[42,43] functionalized-MXene,[44] metal-organic framework materials, and metal oxide@carbon matrixes are considered to be effective lithiophilic 3D scaffolds.[45,46]

However, the rational design of lithiophilic 3D scaffolds is normally accompanied by a costly and complex manufacturing process. For example, Tao et al. used five steps to prepare a lithiophilic ZnO@HPC scaffold.[47] Even though such as-prepared Li metal anodes can achieve satisfactory electrochemical performance, their practical application is greatly limited. Therefore, it is necessary to develop a facile and cost-effective

[a] X. Qian, D. Miao, Dr. J. Qu
     College of Chemistry and Chemical Engineering
     Hunan Normal University
     410081, Hunan, China
     E-mail: qujie@hunnu.edu.cn
[b] X. Qian, X. Tu, Prof. C. Lai
     School of Chemistry and Materials Science
     Jiangsu Normal University
     221116, Jiangsu, China
     E-mail: tuxingchao@jsnu.edu.cn
            laichao@jsnu.edu.cn
[c] X. Lin, M. Chen, Y. Xie
     Ningde Amperex Technology Limited
     352100, Fujian, China

Batteries & Supercaps

Research Article
doi.org/10.1002/batt.202200161

Chemistry
Europe
European Chemical
Societies Publishing

approach to producing lithophilic 3D porous conductive electrode materials.

In this study, a facile infiltration method was adopted to prepare a lithiophilic SnO_2@graphite fiber (SnO_2@GF) electrode. Commercial three-dimensional GF was employed, and the lithiophilic SnO_2 coating layer was simply produced via infiltration and an annealing process, which satisfactorily addressed the problem of practicality. Moreover, the obtained 3D architecture of lithiophilic SnO_2 could control Li deposition and accommodate the volume changes during cycling to achieve a high cycling stability.

Results and Disscussion

Schematic diagrams of the metal oxide@GF synthesis and Li plating processes are displayed in Figure 1(a). Following the annealing process, SnC_2O_4 was converted to SnO_2, which was evenly coated on the surface of the carbon fiber and induced the uniform deposition of Li metal. Such a mechanism of

coating and lithium deposition was confirmed by the results of SEM images and EDS mapping. As shown in Figure 1(b and c), a thin and uniform coating layer could be observed through the cracked regions. This was also clearly identified from the cross-sectional morphology of the obtained composite and the corresponding EDS mapping (Figure 1e–g). DFT calculations were performed to investigate the interactions between the lithiophilicity of SnO_2 with Li ions and of C with Li ions. The results are shown in Figure 1(h–j). It is worth noting that C provided a limited binding energy of only 0.99 eV. However, a high binding energy of 2.5 eV was obtained for SnO_2, which revealed a strong interaction between the Li ions and SnO_2, thus offering preferential nucleation sites of metal Li. Owing to the lithiophilicity of SnO_2, homogeneous deposition of Li metal on the surface of the composite fiber, but not on the surface of the electrode, was easily achieved, as shown in Figure 1(d).

The effects of different amounts of SnC_2O_4 and different metal oxides on the morphology of the composite material were also investigated. As shown in Figure S1, when the quantity of SnC_2O_4 was increased to 0.2066 g, some of the
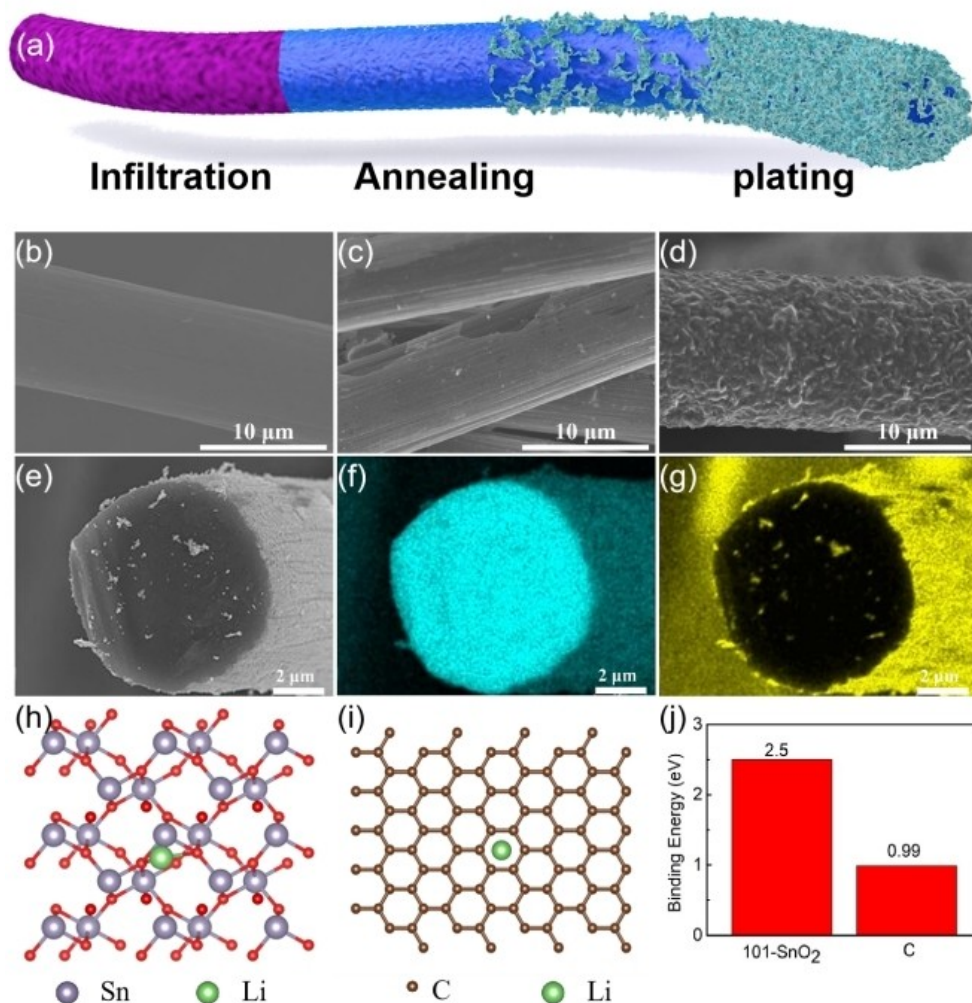

Figure 1. a) Schematic diagrams of metal oxide@GF synthesis and Li plating processes. SEM images of b) bare GF, c) SnO_2@GF-1 and d) SnO_2@GF-1 plated with a capacity of 2 mAh cm^{-2}. SEM image of e) SnO_2@GF-1 from cross section view and EDS mappings of f) C and g) Sn. Top-view simulation images of the distribution of electrodeposition Li atoms on h) SnO_2 and i) bare C. j) The calculated binding energies for SnO_2 and C.

Batteries & Supercaps

Research Article
doi.org/10.1002/batt.202200161

Chemistry Europe
European Chemical
Societies Publishing

formed SnO_2 was accumulated on the GF surface. The SEM images and EDS mappings of Fe_2O_3@GF, Co_3O_4@GF, and NiO@GF are presented in Figure S2. Unfortunately, despite using the same ratios, even coatings of Fe_2O_3, Co_3O_4, and NiO could not be obtained; obvious agglomeration of the metal oxide occurred. Uneven coatings aggravate the uneven deposition of metallic lithium, especially during long-term cycling. Thus, the composite with the lower SnO_2 content (SnO_2@GF-1) was chosen as the carrier for the Li metal composite electrode.

The XRD patterns of SnO_2@GF are shown in Figure 2(a). All peaks can be assigned to tetragonal rutile SnO_2 (JCPDS card no. 41-445) and graphite, regardless of the content of SnO_2. The generation of crystalline Fe_2O_3, Co_3O_4, and NiO was also detected, as shown in Figure S3, corresponding to pure α-Fe_2O_3 (JCPDS card no. 33-0664), Co_3O_4 (JCPDS card no. 43-1003), and cubic NiO (JCPDS card no. 43-1003), respectively. To confirm the content of metal oxide, TGA was carried out (Figures 2b and S4). The weights of all samples decreased over the temperature range 500–800 °C, which resulted from the decomposition of the GF. The SnO_2 content of SnO_2@GF-1 and SnO_2@GF-2 was 11.46% and 27.75%, respectively. The Fe_2O_3 content for Fe_2O_3@GF was 18.8%. However, the loading content was only 1.5% and 3.5% for Co_3O_4 and NiO, respectively. The different morphologies and compositions may have resulted from the different mechanisms of thermal decomposition and interactions between the carbon fiber and the different metal oxides. The low content and uneven distribution of lithiophilic materials did not satisfactorily

regulate the deposition of metallic lithium.[40,46] XPS was further employed in order to explore the surface elemental composition and valence states of SnO_2@GF-1. The high-resolution O 1s spectrum is presented in Figure 2(c). The peak at approximately 531.2 eV was assigned to the Sn–O bond, whereas the other two peaks at 532.1 and 533.2 eV corresponded to the C=O and C–O bonds, respectively. In Figure 2(d), the Sn 3d spectrum is presented with two fitted peaks at 487.5 and 495.8 eV corresponding to the Sn $3d_{5/2}$ and Sn $3d_{3/2}$ of Sn^{4+}, respectively.[18,19]

The strong regulatory effect of SnO_2@GF-1 on Li deposition was first investigated via plating experiments in symmetric cells. As shown in Figure 3(a), with a Li loading of 2 mAh cm^{-2}, uniform deposition was observed for bare GF, whereas a higher Li loading of 4 mAh cm^{-2} resulted in the appearance of protuberances on the surface (Figure 3c). Additionally, it is clear that Li metal accumulated randomly, resulting from the rough and heterogeneous surface of the GF, as presented by the cross-sectional view (Figure 3b and d). The SEM images of the bare GF with Li loadings of 6 and 8 mAh cm^{-2} are shown in Figure S5, and it can be seen that severely uneven aggregation occurred. In direct contrast, a smooth and uniform Li layer was formed on SnO_2@GF-1, with no accumulation of Li observed, even at Li loading of up to 6 mAh cm^{-2} (Figure 3e–j). When the Li loading was further increased to 8 mAh cm^{-2}, partial accumulation appeared, indicating that the maximum plating capacity was approximately 6 mAh cm^{-2} (Figure 3k and l). For
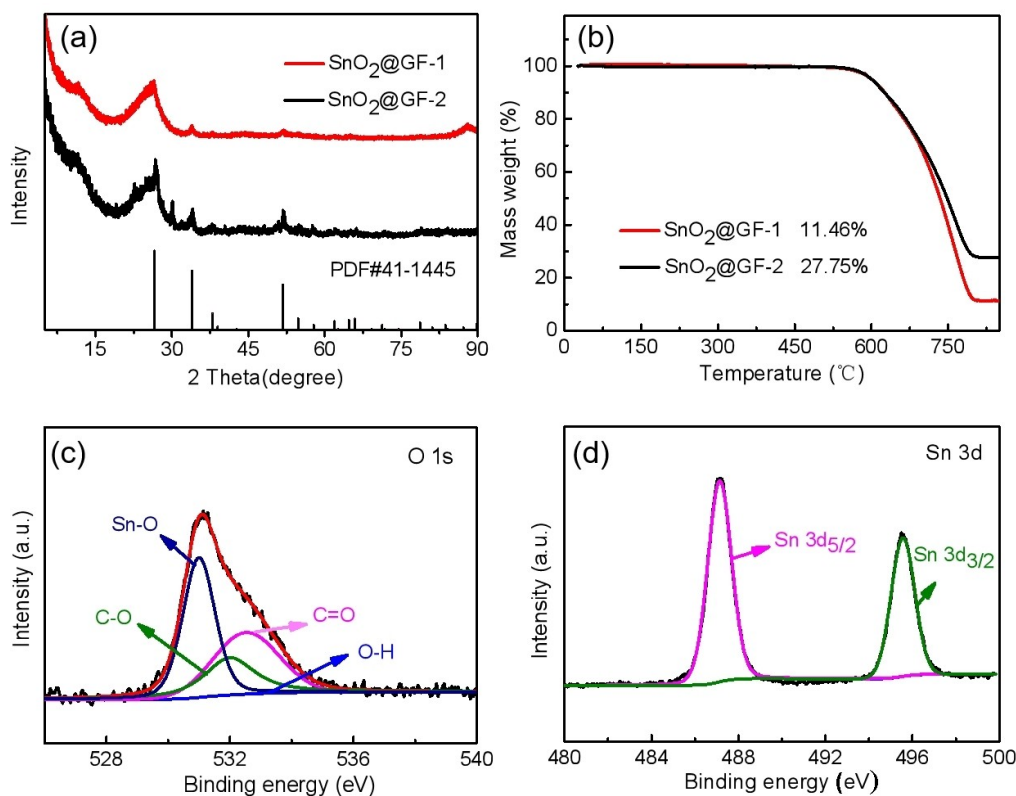

Figure 2. a) XRD pattern and b) TGA analysis of SnO_2@GF-1 and SnO_2@GF-2. XPS spectra of SnO_2@GF-1 of c) O1s region and d) Sn3d region.
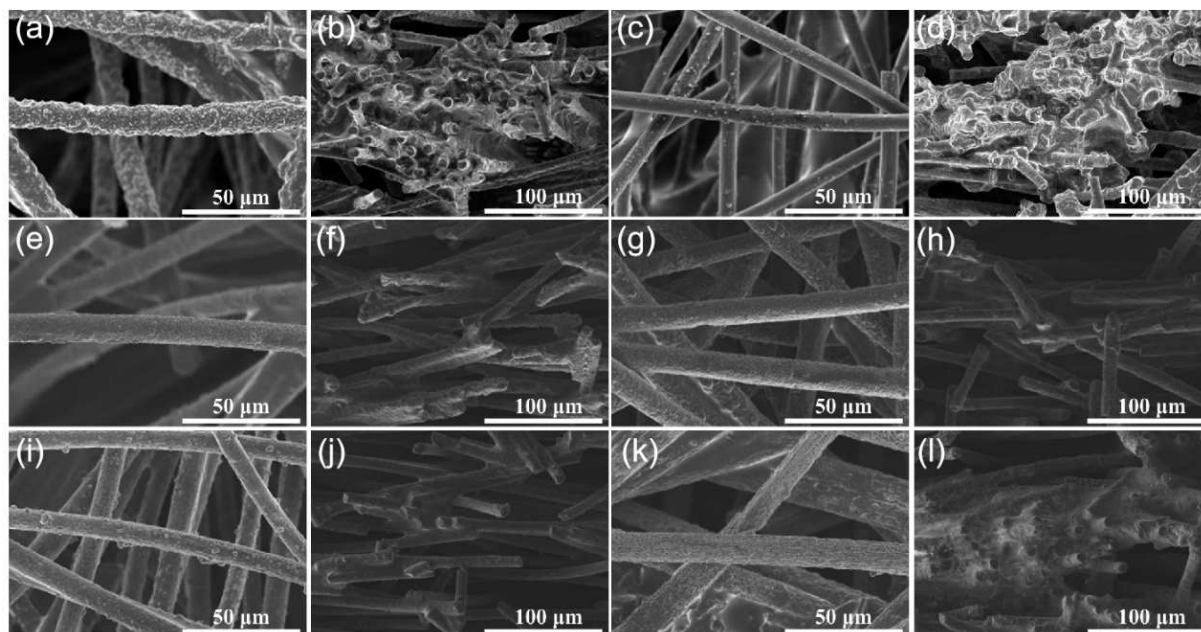
Figure 3. SEM images of GF with plating capacity of a, b) 2 and c, d) 4 mAh cm^{-2}. SEM images of SnO$_2$@GF-1 plated with a capacity of e, f) 2, g, h) 4, i, j) 6 and k, l) 8 mAh cm^{-2}. a, c, e, g, i and k) from surface view; b, d, f, h, j and l) from cross-sectional view.

comparison, SEM images of SnO$_2$@GF-2 plated with different Li loadings are also presented in Figure S6.

Accordingly, the Li@SnO$_2$@GF-1 electrodes were first prepared by plating at an areal capacity of 6 mAh cm^{-2} of Li metal. As compared to GF electrode (Figure S7), Li$^+$ reacts preferentially with SnO$_2$ to induce the uniform nucleation of metal Li

during further plating, thus offering a better cycling stability. Subsequently, their electrochemical properties were then tested in symmetric cells at a current density of 3 mA cm^{-2} with a plating capacity of 3 mA cm^{-2}. As shown in Figure 4(a and b), a high CE, which was close to 100% in the initial cycles, was obtained for Li@SnO$_2$@GF-1, even after 400 cycles. In contrast,
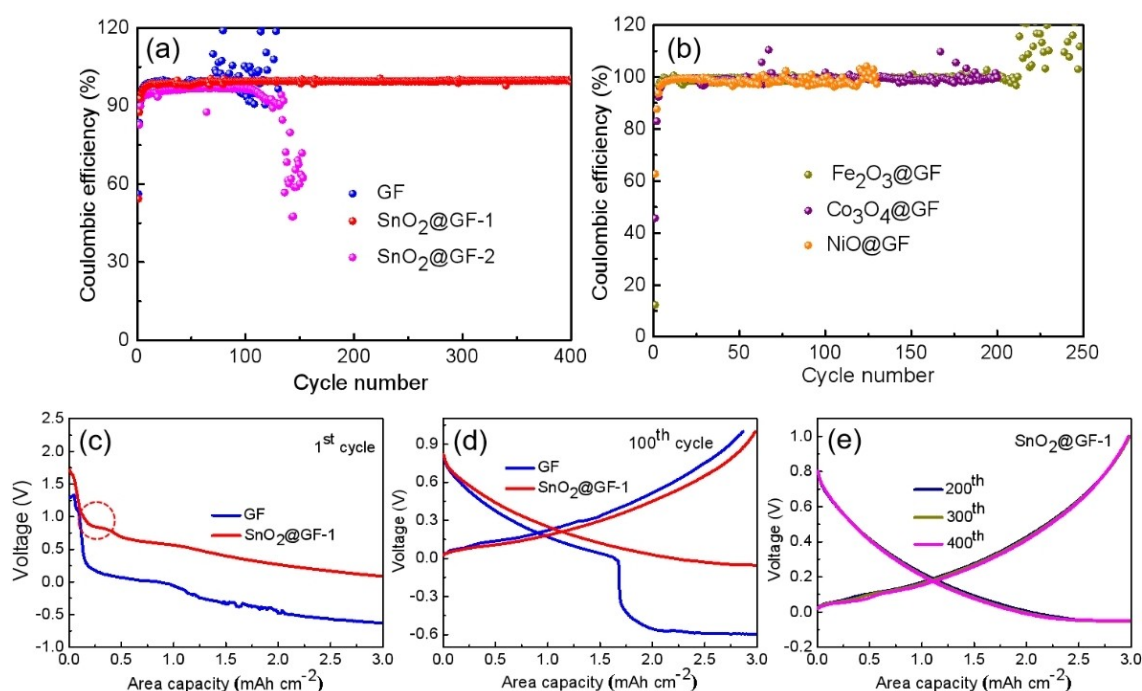

Figure 4. The Coulombic efficiency of symmetrical cells using different anodes with a capacity of 3 mAh cm^{-2} at a current density of 3 mA cm^{-2} of a) SnO$_2$@GF-1, SnO$_2$@GF-2 and GF, b) Fe$_2$O$_3$@GF, Co$_3$O$_4$@GF and NiO@GF. Voltage profiles of c) 1st cycle for SnO$_2$@GF-1 and GF anodes, d) 100th cycle for SnO$_2$@GF-1 and GF anodes and e) 200th, 300th and 400th for SnO$_2$@GF-1 anode.

Batteries & Supercaps

Research Article
doi.org/10.1002/batt.202200161

Chemistry Europe
European Chemical
Societies Publishing

dramatic fluctuations of Li@GF are observed after only 60 cycles. Such fluctuations can be ascribed to partial short circuits that are caused by the formation of Li dendrites through overconsumption of Li metal and electrolyte in the discharging/charging process.[21] In addition, the Li@SnO$_2$@GF-2 electrode retained a CE above 95% for 100 cycles, and then decayed rapidly and fluctuated, indicating short-circuit happening. The voltage profiles of the Li plating/stripping processes for Li@SnO$_2$@GF-1 and Li@GF are shown in Figure 4(c–e). A nucleation overpotential for Li@SnO$_2$@GF-1 in the first cycle is shown in Figure 4(c), which indicates the preferential reaction between Li metal and SnO$_2$, followed by continuous deposition of Li. Such a result implies that SnO$_2$ plays an important role during the Li nucleation stage. For comparison, the CEs of Li@Fe$_2$O$_3$@GF, Li@Co$_3$O$_4$@GF, and Li@NiO@GF are also shown in Figure 4(b). Li@Fe$_2$O$_3$@GF displayed the best cycling stability; however, obvious fluctuations occurred just after 200 cycles, much poorer than the Li@SnO$_2$@GF-1 electrode. To reveal the difference in electrochemical performance, the binding energies of the three metal oxides were calculated. As presented in Figure S8, the binding energy of Fe$_2$O$_3$ and Co$_3$O$_4$ is higher than that of SnO$_2$, corresponding to a better lithiophilicity. Thus, the different performance may be mainly caused by uneven coating. As shown in Figures 1 and 3, uniform coating layer was obtained for SnO$_2$@GF, while for other composite materials, agglomeration of metal oxides can be observed, which may

induce the uneven deposition of metal Li and a poor cycling life.

The Li@SnO$_2$@GF-1 (6 mAh cm^{-2}) anode was then paired with the NCM811 cathode. For comparison, a full cell with a Li@GF anode was also assembled. The rate performance is presented in Figure 5(a), and the corresponding discharging/charging curves are displayed in Figures 5(b) and S9. High specific capacities, of approximately 148, 121, 109, and 85 mAh g^{-1} with the Li@SnO$_2$@GF-1 anode at 0.5, 1, 2, and 5 C, respectively, were achieved. More importantly, Li@SnO$_2$@GF-1 also showed excellent rate performance at higher current densities of 2 and 5 C, at which the capacities remained stable. When the current rate was returned to 2 C, the discharge capacity recovered to 109 mAh g^{-1}. However, Li@GF experienced a serious decay in capacity during the cycling.

The long-term cycling performance of the two full cells at a current density of 5 C is shown in Figure 5(c). The Li@SnO$_2$@GF-1||NCM811 full cell had a stable, long cycle performance, with the discharging capacity maintained above 80 mAh g^{-1} after 200 cycles. A high CE of approximately 100% over the entire series of cycles was observed. However, the Li@GF||NCM811 full cell suffered a serious capacity decay from about the 50th cycle onward, which indicated a rapid capacity decay for Li@GF caused by Li dendrites, followed with a short-circuited battery.

The interfacial properties of the full cells were investigated by EIS. As shown in Figure 5(d), all the Nyquist plots contained depressed semicircles and inclined lines. The semicircle at high
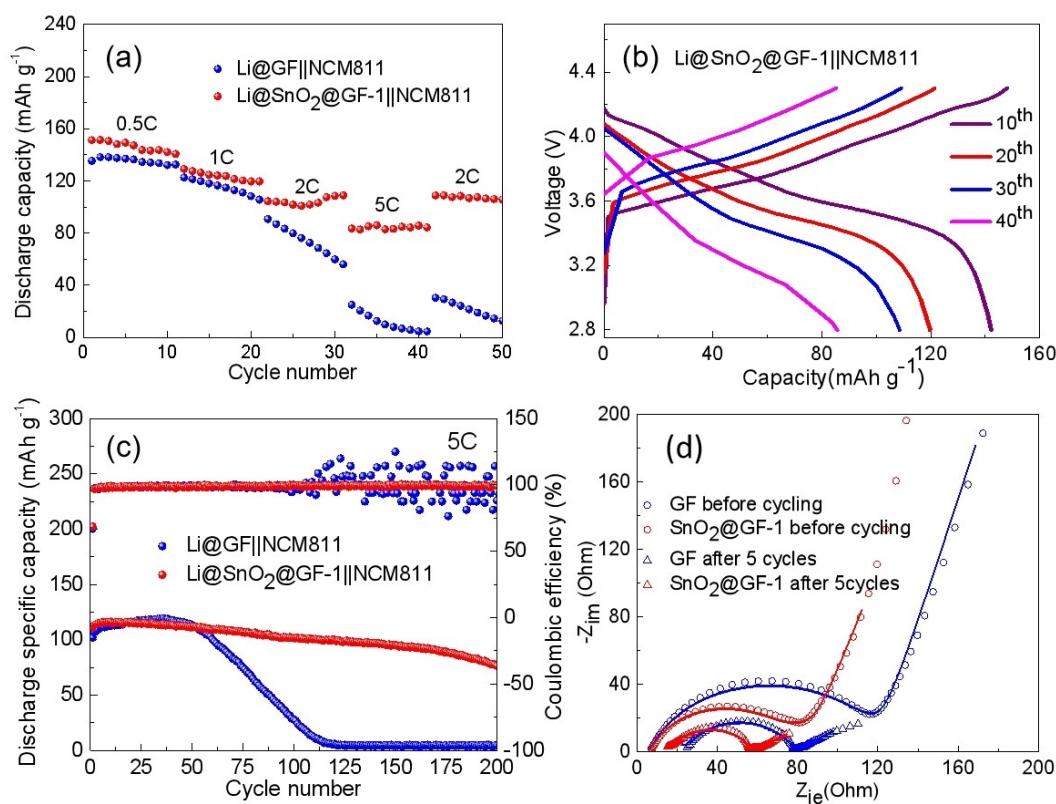

Figure 5. a) Rate capability of Li@SnO$_2$@GF-1||NCM811 and bare Li@GF||NCM811 full cells at varied current densities; b) discharging/charging curves at varied current densities; c) cycling performance and Coulombic efficiency at 5 C; d) EIS spectra before and after cycling and the fitted results.
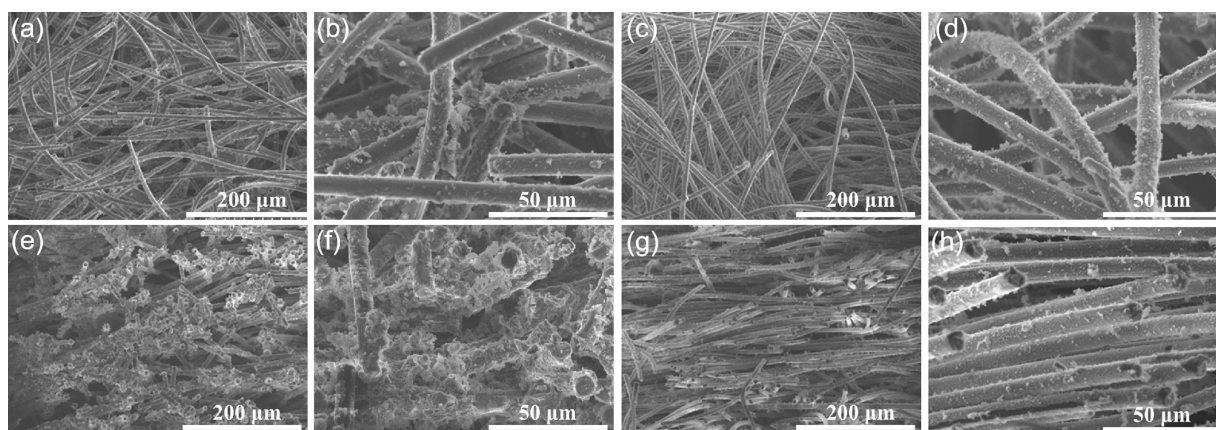
Figure 6. SEM images of bare Li@GF anode after 200 cycles at the current density of 5 C from a, b) surface view and e, f) cross-sectional view; SEM images of Li@SnO$_2$@GF-1 anode after 200 cycles at the current density of 5 C from c, d) surface view and g, h) cross-sectional view

frequencies corresponded to the interfacial resistance between the electrolyte/electrode and the charge transfer resistance at the electrode surface.[38] The Nyquist plots were fitted with the equivalent circuit model (Figure S10), and the experimental data are listed in Table S1. A large interfacial resistance, of approximately 113.4 Ω for the bare Li@GF anode, was observed before cycling. After five cycles, the resistance was reduced to 53.6 Ω. Li@SnO$_2$@GF-1 had a small interfacial resistance, of approximately 57.7 Ω, which was reduced to 39.7 Ω after five cycles, indicating superior Li stripping/plating kinetics and stable cycling.

The cycled Li@SnO$_2$@GF-1 and Li@GF anodes were removed from the full cells to further examine the modifications that had occurred. SEM was used to observe the surface morphology of the corresponding anodes after 200 cycles. The unexpected formation and growth of Li dendrites on the Li@GF anode was found at the junction of the GF (Figure 6a and b). In addition, as seen from the cross-sectional images shown in Figure 6(e and f), the inside space of the electrodes was filled with Li dendrites, which may have led to the battery failure. However, no Li dendrites were found in the Li@SnO$_2$@GF-1 electrode, as shown in Figure 6(c, d, g, and h), providing further confirmation that the growth of Li dendrites can be inhibited effectively, resulting in superior, stable, long cycling performance.

Conclusions

In summary, we successfully prepared lithiophilic SnO$_2$@GF material as a Li host for producing highly stable Li composite anodes. Characterization and DFT calculations showed that 3D-structured lithiophilic SnO$_2$@GF material can regulate the electric field distribution efficiently, reduce the local current density, and promote uniform Li nucleation during plating. Combined with a highly conductive porous framework, no Li dendrites were produced during charge/discharge cycling, and superior, stable long-cycling performance was obtained in both symmetric and full cells. In particular, the Li@SnO$_2$@GF electro-

des that we prepared displayed a high CE, of approximately 100% over up to 400 cycles, even at a current density of 3 mA cm^{-2} with a high plating capacity of 3 mAh cm^{-2}. These outstanding results promote lithiophilic SnO$_2$@GF as a prospective matrix for the construction of efficient lithium metal anodes. In addition, involving facile and cost-effective approaches, such as the use of commercial GF materials and a simple infiltration method, these lithiophilic SnO$_2$@GF electrodes provide new insights into the practical applications of lithium metal anodes.

Experimental Section

Tin oxalate (SnC$_2$O$_4$, 0.1033 g) was dissolved in 80% ethanol (20 mL). Graphite fiber (GF) (4 cm×3 cm×1 mm) was then soaked in the above solution for 10 min and subsequently sonicated for 30 s. After drying at 60 °C overnight, the above product was calcined at 500 °C under an argon atmosphere for 5 h. Finally, the sintered material (SnO$_2$@GF-1) was cut into round pieces (diameter 10 mm). The method used to prepare SnO$_2$@GF-2 was identical to that used for the synthesis of SnO$_2$@GF-1, except that a different mass of tin oxalate (0.2066 g) was used. Fe$_2$O$_3$@GF, Co$_3$O$_4$@GF, and NiO@GF were prepared by the same method. The process of plating was realized through galvanostatic discharge. The plating capacity can be identified by the discharge time. Specifically, when plating 2 mAh cm^{-2} of Li at a current density of 0.5 mA cm^{-2}, the discharge time was 4 h.

The X-ray powder diffraction patterns of the samples were obtained on a Bruker D8 Advance X-ray diffractometer (Cu K_α= 15.4056 nm; Bruker, Berlin, Germany). A scanning electron microscope (SEM, SU8200, Hitachi High-Technologies Corporation, Tokyo, Japan) was used to characterize the sample morphology. Energy-dispersive X-ray spectroscopy (EDS) mapping analysis was also conducted on the Hitachi SU8200. Thermal gravimetric analysis (TGA, STA 449 F5 Jupiter, NETZSCH Holding, Selb, Germany) was performed under an air atmosphere at a rate of 10 °C min^{-1}. X-ray photoelectron spectroscopy (XPS) data were obtained using an ESCALAB250Xi (Thermo Fisher, Waltham, MA, USA) with a monochromatized Al K standard X-ray source.

Density functional theory (DFT) calculations were performed using the Vienna Ab initio Simulation Package (VASP). The general

Batteries & Supercaps

Research Article
doi.org/10.1002/batt.202200161

Chemistry
Europe
European Chemical
Societies Publishing

gradient approximation (GGA) of Perde-Burke-Ernzerdof (PBE) was employed for the exchange-correlation function. The electron-ion interactions were described using the projector augmented wave (PAW) method. The plane wave basis set, which included a kinetic cut-off energy, was 520 eV. The Brillouin zones were sampled on a grid of $4\times4\times1$ gamma special k-points for the graphene surface and a grid of $2\times3\times1$ gamma special k-points for the SnO_2 (101) surface. A vacuum space of 15 Å in the direction vertical to the model slab was set in order to avoid any interactions between the periodically repeated images. For the SnO_2 (101) supercell, the top two layers were allowed to fully relax, while the bottom three layers were fixed. The geometric optimization was terminated when the forces on all unconstrained atoms were less than $0.02\ eV\ \text{Å}^{-1}$.

The adsorption energy (E_{ads}) of the Li atoms on the surfaces was computed from the equation: $E_{ads}=E_{Total}-E_{Slab}-E_{Li}$ where E_{Total}, E_{Slab}, and E_{Li} represent the total energy of the adsorption system, the isolated Li atom and of the summation of the adsorbed system, the model slab and the Li atom adsorbate, respectively.

For symmetric cells, the synthesized materials were used as the working electrode and lithium foil was used as the counter electrode. The loading mass of electrode is $1.5\ mg\ cm^{-2}$. The electrolyte used in the symmetric cells was composed of 1.0 M lithium bis(trifluoromethanesulfonyl)-imide (LiTFSI) dissolved in a mixture of dimethoxyethane (DME) and dioxolane (DOL) at a volume ratio of 1:1 with 0.2 M lithium nitrate. Full cells were assembled with a $LiNi_{0.8}Co_{0.1}Mn_{0.1}O_2$ (NCM811) cathode in an Ar-filled glove box. The cathodes were prepared by mixing the NCM811, super P carbon black, and poly(vinylidene difluoride) (PVDF) binder (weight ratio of 7:2:1) with N-methyl-2-pyrrolidine (NMP) as the solvent. The loading active material of NCM811 is $2.5\ mg\ cm^{-2}$. The slurry was pasted onto aluminum foil and dried at 60°C for 12 h in a vacuum. A solution of 1 M lithium hexafluorophosphate ($LiPF_6$) in an ethylene carbonate (EC)/dimethyl carbonate (DEC)/diethyl carbonate (DMC) mixture (volume ratios 1:1:1) was used as the electrolyte. And the adding amount of electrolyte is 100 µL.

The electrochemical performance was tested using a LAND CT2001 A battery test system (Wuhan Jinnuo Electronics, Ltd., Wuhan, China). The anodes used in the full cells were pre-deposited at $6\ mAh\ cm^{-2}$ at a current density of $0.5\ mAh\ cm^{-2}$. The assembled full cells were cycled between 2.8 and 4.3 V versus Li^+/Li. Electrochemical impedance spectroscopy (EIS) was used to obtain spectra in the frequency range between 0.01 Hz and 100 kHz.

Conflict of Interest

The authors declare no conflict of interest.

Data Availability Statement

The data that support the findings of this study are available from the corresponding author upon reasonable request.

[1] D. Lin, Y. Liu, Y. Cui, *Nat. Nanotechnol.* **2017**, *12*, 194–206.
[2] J. B. Goodenough, K.-S. Park, *J. Am. Chem. Soc.* **2013**, *135*, 1167–1176.
[3] J. l. Lee, G. Song, S. Cho, D. Y. Han, S. Park, *Batteries & Supercaps* **2020**, *3*, 828–859.
[4] P. Albertus, S. Babinec, S. Litzelman, A. Newman, *Nat. Energy* **2018**, *3*, 16–21.
[5] X. Hou, S. Xue, M. Liu, X. Shang, Y. Fu, D. He, *Chem. Eng. J.* **2018**, *350*, 29–36.
[6] J. Xie, J. Ye, F. Pan, X. Sun, K. Ni, H. Yuan, X. Wang, N. Shu, C. Chen, Y. Zhu, *Adv. Mater.* **2019**, *31*, 1805654.
[7] K. R. Adair, M. Iqbal, C. Wang, Y. Zhao, M. N. Banis, R. Li, L. Zhang, R. Yang, S. Lu, X. Sun, *Nano Energy* **2018**, *54*, 375–382.
[8] J. W. Choi, D. Aurbach, *Nat. Rev. Mater.* **2016**, *1*, 16013.
[9] M. M. Thackeray, C. Wolverton, E. D. Isaacs, *Energy Environ. Sci.* **2012**, *5*, 7854–7863.
[10] W. Xu, J. Wang, F. Ding, X. Chen, E. Nasybulin, Y. Zhang, J.-G. Zhang, *Energy Environ. Sci.* **2014**, *7*, 513–537.
[11] P. G. Bruce, S. A. Freunberger, L. J. Hardwick, J.-M. Tarascon, *Nat. Mater.* **2012**, *11*, 19–29.
[12] Y. X. Zhan, P. Shi, X. X. Ma, C. B. Jin, Q. K. Zhang, S. J. Yang, B. Q. Li, X. Q. Zhang, J. Q. Huang, *Adv. Energy Mater.* **2021**, *12*, 2103291.
[13] Y. Guo, H. Li, T. Zhai, *Adv. Mater.* **2017**, *29*, 1700007.
[14] B. Li, Y. Wang, S. Yang, *Adv. Energy Mater.* **2018**, *8*, 1702296.
[15] Y. Liu, Z. Ju, B. Zhang, Y. Wang, J. Nai, T. Liu, X. Tao, *Acc. Chem. Res.* **2021**, *54*, 2088–2099.
[16] A. Zhamu, G. Chen, C. Liu, D. Neff, Q. Fang, Z. Yu, W. Xiong, Y. Wang, X. Wang, B. Z. Jang, *Energy Environ. Sci.* **2012**, *5*, 5701–5707.
[17] Y. Gu, W.-W. Wang, Y.-J. Li, Q.-H. Wu, S. Tang, J.-W. Yan, M.-S. Zheng, D.-Y. Wu, C.-H. Fan, W.-Q. Hu, *Nat. Commun.* **2018**, *9*, 1339.
[18] Y. Zhao, L. P. Wang, S. Xi, Y. Du, Q. Yao, L. Guan, Z. J. Xu, *J. Mater. Chem. A* **2017**, *5*, 25609–25617.
[19] Y. Yang, X. Zhao, H.-E Wang, M. Li, C. Hao, M. Ji, S. Ren, G. Cao, *J. Mater. Chem. A* **2018**, *6*, 3479–3487.
[20] Z. Yan, H.-Y. Pan, J.-Y. Wang, R.-S. Chen, Q. Li, F. Luo, X.-Q. Yu, Hong Li, *Rare Met.* **2021**, *40*, 1357–1365.
[21] G. Huang, P, Guo, J. Wang, S. Chen, J. Liang, R. Tao, S. Tang, X. Zhang, S. Cheng, Y.-C. Cao, S. Dai, *Chem. Eng. J.* **2018**, *384*, 123313.
[22] Q. Wang, C. Yang, J. Yang, K. Wu, C. Hu, J. Lu, W. Liu, X. Sun, J. Qiu, H. Zhou, *Adv. Mater.* **2019**, *31*, 1903248.
[23] K. Chen, R. Fang, Z. Lian, X. Zhang, P. Tang, B. Li, K. He, D.-W. Wang, H.-M. Cheng, Z. Sun, *Energy Storage Mater.* **2021**, *37*, 224–232.
[24] F. Li, J. Li, F. Zhu, T. Liu, B. Xu, T.-H. Kim, M. J. Kramer, C. Ma, L. Zhou, C.-W. Nan, *Matter* **2019**, *1*, 1001–1016.
[25] T. Deng, X. Ji, Y. Zhao, L. Cao, S. Li, S. Hwang, C. Luo, P. Wang, H. Jia, X. Fan, *Adv. Mater.* **2020**, *32*, 2000030.
[26] H. Yang, J. Li, Z. Sun, R. Fang, D.-W. Wang, K. He, H.-M. Cheng, F. Li, *Energy Storage Mater.* **2020**, *30*, 113–129.
[27] X. Liu, X. Qian, W. Tang, H. Luo, Y. Zhao, R. Tan, M. Qiao, X. Gao, Y. Hua, H. Wang, *J. Energy Chem.* **2021**, *52*, 385–392.
[28] X. Qian, X. Fan, Y. Peng, P. Xue, C. Sun, X. Shi, C. Lai, J. Liang, *Adv. Funct. Mater.* **2021**, *31*, 2008044.
[29] S. Wang, L. Zhou, M. K. Tufail, L. Yang, P. Zhai, R. Chen, W. Yang, *Chem. Eng. J.* **2021**, *415*, 128846.
[30] D. Kang, S. Sardar, R. Zhang, H. Noam, J. Chen, L. Ma, W. Liang, C. Shi, J. P. Lemmon, *Energy Storage Mater.* **2020**, *27*, 69–77.
[31] Y. Liu, Y. Wu, J. Zheng, Y. Wang, Z. Ju, G. Lu, O. Sheng, J. Nai, T. Liu, W. Zhang, X. Tao, *Nano Energy* **2021**, *82*, 105723.
[32] Y. Xiao, R. Xu, L. Xu, J.-F. Ding, J.-Q. Huang, *Energy Mater.* **2021**, *1*, 100013.
[33] M. Chen, J. Zheng, Y. Liu, O. Sheng, Z. Ju, G. Lu, T. Liu, Y. Wang, J. Nai, Q. Wang, X. Tao, *Adv. Funct. Mater.* **2021**, *31*, 2102228.
[34] R. Xu, J. F. Ding, X. X. Ma, C. Yan, Y. X. Yao, J. Q. Huang, *Adv. Mater.* **2021**, *33*, 2105962.

Batteries & Supercaps

Research Article
doi.org/10.1002/batt.202200161

Chemistry Europe
European Chemical
Societies Publishing

[35] B. Zhang, H. Shi, Z. Ju, K. Huang, C. Lian, Y. Wang, O. Sheng, J. Zheng, J. Nai, T. Liu, Y. Jin, Y. Liu, C. Zhang, X. Tao, *J. Mater. Chem. A* **2020**, *8*, 26045–26054.

[36] Y. Liu, X. Tao, Y. Wang, C. Jiang, C. Ma, O. Sheng, G. Lu, X. W. Lou, *Science* **2022**, *375*, 739–745.

[37] T. T. Zuo, X. W. Wu, C. P. Yang, Y. X. Yin, H. Ye, N. W. Li, Y. G. Guo, *Adv. Mater.* **2017**, *29*, 1700389.

[38] X. Yan, L. Lin, X. Han, Z. Qiao, Qi. Xie, J. Lin, Z. Meng, L. Wang, D.-L. Peng, *Chem. Eng. J.* **2021**, *421*, 127872.

[39] J. Chai, B. Chen, F. Xian, P. Wang, H. Du, J. Zhang, Z. Liu, H. Zhang, S. Dong, X. Zhou, *Small* **2018**, *4*, 1802244.

[40] W. Zhang, L. Fan, Z. Tong, J. Miao, Z. Shen, S. Li, F. Chen, Y. Qiu, Y. Lu, *Small Methods* **2019**, *3*, 1900325.

[41] D. Lin, J. Zhao, J. Sun, H. Yao, Y. Liu, K. Yan, Y. Cui, *Proc. Natl. Acad. Sci. Lett.* **2017**, *114*, 4613–4618.

[42] P. Xue, S. Liu, X. Shi, C. Sun, C. Lai, Y. Zhou, D. Sui, Y. Chen, J. Liang, *Adv. Mater.* **2018**, *30*, 1804165.

[43] Z. Li, X. Li, L. Zhou, Z. Xiao, S. Zhou, X. Zhang, L. Li, L. Zhi, *Nano Energy* **2018**, *49*, 179–185.

[44] H. Chen, G. Ke, X. Wu, W. Li, Y. Li, H. Mi, L. Sun, Q. Zhang, C. He, X. Ren, *Chem. Eng. J.* **2021**, *406*, 126775.

[45] W. Liu, Y. Mi, Z. Weng, Y. Zhong, Z. Wu, H. Wang, *Chem. Sci.* **2017**, *8*, 4285–4291.

[46] X.-Y. Yue, J. Bao, S.-Y. Yang, R.-J. Luo, Q.-C. Wang, X.-J. Wu, Z. Shadike, X.-Q. Yang, Y.-N. Zhou, *Nano Energy* **2020**, *71*, 104614.

[47] C. Jin, O. Sheng, J. Luo, H. Yuan, C. Fang, W. Zhang, H. Huang, Y. Gan, Y. Xia, C. Liang, *Nano Energy* **2017**, *37*, 177–186.